Precipitation and reverted austenite formation in maraging 350 steel: competition or cooperation?

A. L. M. Feitosa[a*]; G. G. Ribamar[a]; J. Escobar[a,b]; R. Sonkusare[c,d]; T. Boll[c,d]; F. Coury[e]; J. Ávila[f]; J. P. Oliveira[g]; A. F. Padilha[a]

[a]Department of Metallurgical and Materials Engineering, University of São Paulo (USP), Sao Paulo, Brazil
[b]Currently at the Pacific Northwest National Laboratory, Energy and Environment Directorate, USA
[c]Institute for Applied Materials - Materials Science and Engineering (IAM-WK), Karlsruhe Institute of Technology (KIT), Karlsruhe, Germany
[d]Institute of Nanotechnology (INT), Karlsruhe Institute of Technology (KIT), Eggenstein-Leopoldshafen, Germany
[e]Materials Engineering Department, Federal University of São Carlos (UFSCar), São Carlos, Brazil
[f] Research group in Structures and Mechanics of Materials (REMM), Department of Strength of Materials and Structural Engineering. Universitat Politècnica de Catalunya (UPC), Barcelona, Spain
[g]CENIMAT/I3N, Department of Materials Science, NOVA School of Science and Technology, Universidade NOVA de Lisboa, 2829-516 Caparica, Portugal
[*]Corresponding author: Ana Larissa Melo Feitosa - Department of Metallurgical and Materials Engineering, University of São Paulo (USP). Avenida Professor Mello Moraes, 2463 - 05508-030 São Paulo/SP. larissa.mfeitosa@gmail.com (+5511 959493553)

Abstract

Aged maraging steels offer unique strength and toughness via the presence of finely dispersed precipitates, allowing the material to reach values of up to 2400 MPa in yield strength in the case of 18Ni350. However, when aging heat treatments above 550 °C are conducted, simultaneous precipitation and austenite reversion can occur changing the mechanical behavior of the material. Although many studies related to the physical metallurgy of maraging steels have already been published, less attention has been given to a detailed understanding of the initial formation of austenite and its relationship with the precipitates. In this study, undeformed and cold rolled commercial 18Ni350 maraging steel samples were submitted to short aging heat treatments of 1800 s at 600, 650, and 700 ºC. The influence of the initial microstructure on subsequent phase evolution was studied using in-situ synchrotron X-ray diffraction and final microstructural products using transmission electron microscopy and atom probe tomography. Results show that cold rolled samples did not present faster kinetics of transformation of reverted austenite as expected, but this condition presented austenite in a different morphology than the undeformed condition. However, cold rolling changed the morphology of reverted austenite from elongated (undeformed case) to equiaxed; and induced a higher density of smaller Ni_3Ti and Fe_2Mo precipitates, especially after low-temperature aging. Besides, the deformation extinguished retained austenite, which influenced the reverted austenite formation, concluding that the simple increase in dislocation density is not a unique and direct factor to increase the reverted austenite kinetics.

Keywords
Atom-probe tomography; X-ray synchrotron radiation; Transmission electron microscopy; Phase transformation kinetics; Reverted austenite

1. Introduction

Maraging steels represent a class of Fe-Ni-based alloys with a high dislocation density in a soft lath martensite matrix, where aggregates of laths are organized in blocks and packets [1]. More details of this type of microstructure can be found elsewhere [2] and [3]. These ultrahigh-strength steels attain elevated hardness and mechanical strength through the occurrence of intermetallic precipitation during aging treatments conducted between 455°C and 510°C [4–6]. The substantial presence of alloying elements such as Ni, Ti, Mo, and Co results in the formation of well-known intermetallic nanoprecipitates, with the Ni_3(Ti,Mo) phase being frequently reported [1,7,8].

In addition to intermetallic precipitation, those steels can undergo martensite to austenite reversion under specific time and temperature conditions, resulting in the overaging of the material. Austenite reversion is of particular significance in maraging steels as its presence contributes to recovery and increases ductility [4,7,9,10]. The formation of reverted austenite occurs through the enrichment of gamma (γ) stabilizer elements in the previous austenite grain and lath/lath boundaries and defects facilitated by pipe diffusion, i.e., diffusion along dislocations [4,11]. This mechanism is commonly observed in precipitation hardening (PH) maraging steels, stainless steels, and Fe-Ni alloys [3,12–15]. Seemingly, plastic deformation is a factor that can assist austenite reversion, by increasing the dislocation density and accelerating the phase transformations in maraging steels [7,16]. Nevertheless, limited research has delved into

this aspect, with the investigation conducted by Ali et al. [16] serving as the foundational basis of such affirmation in other works.

It has been commonly reported that both precipitation and austenite reversion are diffusion-controlled mechanisms in maraging 300 and 350 steels [17–20]. However, it has been already demonstrated by other authors that, depending on the alloy composition and heat treatment temperature, austenite formation can potentially change from diffusive to massive/martensitic [3,13,21]. Classical literature often describes precipitation and austenite reversion as a sequence of dissolution and formation [1,4,8,22], focusing on each transformation and disregarding the possibility of mechanistic overlap. Other researchers have affirmed that aging 18Ni350 at temperatures higher than 640 °C alter the transformation sequence, with reverted austenite forming before precipitation [23]. Moreover, thermodynamic and kinetic simulations, performed by Schnitzer et al. [12], indicated that NiAl precipitates and reverted austenite nucleated simultaneously and independently in PH 13-8 Maraging steels. Therefore, it becomes challenging to discern whether the precipitates and the reverted austenite cooperate or compete during conventional heat treatment cycles, and in situ characterization becomes essential to clearly deconvolute compositional and thermal factors.

This study aims to understand the sequence and possible relation of intermetallic precipitation and austenite reversion in an undeformed and a 50% cold rolled maraging 350 steel during overaging heat treatments. For that, in-situ synchrotron X-ray diffraction to quantify reverted austenite evolution during overaging treatments at 600, 650, and 700 °C. Transmission electron microscopy and atom probe tomography were used for detailed analysis of microstructural products, such as Ni_3Ti, Fe_2Mo, and

austenite. Moreover, the influence of cold rolling on the reverted austenite kinetics and morphology, and intermetallic precipitates distribution was investigated.

2. Materials and Methods

A commercial maraging 350 steel furnished by Villares Metals S/A produced through a sequence involving a vacuum induction melting (VIM) furnace and a vacuum arc remelting (VAR) furnace, was used in this investigation. Following these manufacturing stages, the material underwent a process of hot forging and solution annealing at 820 °C for 1 hour. Subsequently, the material was subjected to machining to attain a cylindrical billet configuration with a diameter of 17 cm, after which it was sectioned into disks with a width of 20 mm. The bulk composition, as provided by the supplier, is in Table 1.

In the metallography laboratory of the Department of Metallurgical and Materials Engineering at the University of São Paulo (USP), Brazil, 60x20x20 mm specimens were extracted from the disks in the radial orientation utilizing a Mesotom Struers cutting machine. Subsequently, half of the specimens underwent cold rolling at the *Instituto de Pesquisas Tecnológicas* (IPT - USP), Brazil, employing a semi-industrial rolling mill to achieve a 50% reduction in width. The resulting material was categorized into two distinct initial conditions: as forged with no prior deformation (designated as "F" throughout this manuscript) and those subjected to deformation by cold rolling (designated as "D"). Following this, cylinders measuring 4 mm in diameter and 10 mm in length were precision-machined via wire electrical discharge machining (EDM). The cylindrical specimens of the "D" condition were extracted in alignment with the rolling direction.

Table 1 - Maraging 350 steel grade composition. (*x10^{-3})

	Ni	Co	Mo	Ti	Al	Cr	Si	Mn	C*	Fe
at. %	17.53	11.84	2.89	1.69	0.21	0.04	0.04	0.03	2.40	Bal.
wt. %	17.85	12.10	4.80	1.40	0.10	0.04	0.02	0.03	0.05	Bal.

In-situ synchrotron X-ray diffraction (SXRD) was carried out at the P07 beamline at the Deutsches Elektronen-Synchrotron (DESY) in Hamburg, Germany. The beamline is equipped with a modified Bähr DIL 805 A/D dilatometer. A beam energy of ≈ 87 keV (λ = 0.14235 Å) was used, allowing diffraction in transmission geometry. The calibration pattern used was a LaB_6 sample. Overaging heat cycles were conducted at 600, 650, and 700 °C for 1800 s (30 minutes). The heating and cooling rates used were 50 and 10 °C.s^{-1}, respectively. The sample identification was simplified by the temperature of overaging + the initial condition, for instance, the cold rolled sample treated at 600 °C is called 600D. Around 600 diffraction patterns were collected for each heat treatment, and the data acquisition rate was one diffraction pattern every 4 seconds. Therefore, the temperature resolution at the heating step was 100 °C, and at the cooling stage was 40 °C. The diffraction data fitting and phase quantification were done using the methodology presented in previous work [19]. For the quantification of austenite, 5 peaks were used – (200)γ, (200)α', (220)γ, (211)α', and (311)γ – and the calculation was based on the integrated intensity method [24,25]. Due to partial superposition, the peaks (111)γ and (100)α' were not used in the calculation. The concentrations from the SXRD results are given in vol. fraction and vol. %.

Transmission electron microscopy (TEM) images were obtained at the *Laboratório de Caracterização Estrutural* (LCE) at the Federal University of São Carlos (UFSCar), Brazil, using a Tecnai G2 F20 equipment operating with acceleration

tension of 200 kV. Samples were prepared in a Thermo Fisher Scientific Helios NanoLab 660 dual-beam electron microscope equipped with a focused ion beam (FIB) column at the Brazilian Nanotechnology National Laboratory (LNNano). Lift-out thin lamellas of around 8 x 9 μm were produced.

Atom-probe tomography measurements were conducted at the Karlsruhe Institute of Technology (KIT), Germany, in pulsed laser mode using a CAMECA 4000X HR Local Electrode Atom Probe (LEAP) under an ultra-high vacuum and base temperature of 50 K. The detection rate and laser pulse frequency were set at 0.5 % and 125 kHz, respectively. The reconstructions were made using the AP Suite 6.3 software. The composition of the phases from the APT results are given in at. %.

Two APT sample preparation methods were used: FIB and electropolishing. For the former preparation, the lift-out and annular milling technique prepared needle-shaped APT samples using a dual beam FIB equipped in a FEG SEM (Zeiss Auriga 60). For that, the surface was prepared for SEM visualization: ground with sandpaper up to 1200 mesh, then polished with diamond solutions of 3 and 1 μm and etched with Nital solution (10 % nitric acid + 90 % ethanol). For the latter method, a solution of 80 % perchloric acid and 20 % acetic acid was used. To make the electropolishing possible, a specific preparation was needed beforehand: the material was cut with a diamond wire saw to achieve thin long samples of at most 0.3 mm width x 0.3 mm length. These square dowels were connected to copper tubes and attached to a power supply in the abovementioned solution. These were electropolished in the middle part until a neck was formed, and the bottom part of the sample detached, resulting in an upper needle-like part with a nanometric radius. More information regarding this procedure and the FIB method can be found elsewhere [26,27].

3. Results and Discussion

The outcomes are systematically presented in accordance with the experimental procedures conducted. Initial emphasis is placed on the results derived from Synchrotron X-ray Diffraction (SXRD), followed by Transmission Electron Microscopy (TEM) and Electron Backscatter Diffraction (EBSD). This study culminates with the findings obtained through Atom Probe Tomography (APT).

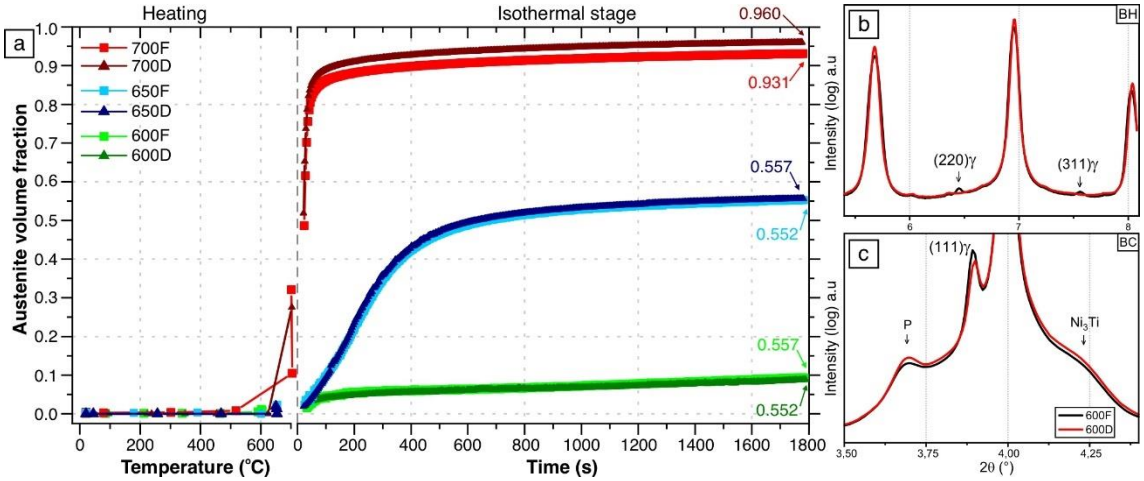

Figure 1 – (a) Evolution of austenite volume fraction along the overaging heat treatments. The values shown are related to the γ quantification at the end of the isothermal step (colors according to the label of the samples). Diffraction patterns of 600F and 600D conditions before heating (b) and before cooling (c).

The evolution of the austenite volume fraction along the overaging heat treatments is depicted in Figure 1a. The initial segment of the graph shows data associated with the heating stage. Austenite growth occurs at around 600 °C during heating for the F condition. This result is consistent with previous study [19].

The evolution of the austenite volume fraction (f_γ) during the isothermal stage is indicated by the vertical dashed line. Notably, there is no significant difference in reversion kinetics between F and D conditions during overaging at 600 and 650 °C. It is only at 700 °C that a slight increase in austenite volume fraction for the deformed condition is evident. The diffusional behavior of the reversion process is indicated by its overall temperature and time dependence, as observed during the overaging treatments.

A careful analysis of the diffractograms before heating (BH in Figure 1b) reveals that the F condition presents a small fraction of retained austenite, which could act as pre-existing nuclei for subsequent austenite growth [28]. This may strongly reduce the activation barrier for nucleation, thereby facilitating austenite reversion. The absence of retained austenite in the D condition supports that this phase was transformed in martensite through plastic deformation, likely due to a Transformation-Induced Plasticity (TRIP) effect [9,29–31].

Moreover, a closer look into the precipitate peaks before cooling (BC), detailed in Figure 1c, suggests enhanced precipitation in the deformed samples compared to the undeformed ones. Upon analyzing the initial formation of austenite in the 700D and 700F samples (Figure 1a), it becomes apparent that the amount of reverted austenite is larger in the deformed condition. Thus, this observation indicates that the introduction of 50 % cold work in a maraging 350 steel may not be enough to directly facilitate austenite formation. Instead, it enhances the nucleation and growth of precipitates, as also demonstrated by Tian et. al. [32].

In Figure 2, the evolution of Full Width at Half Maximum (FWHM) and lattice parameters for the (211) martensite (α') peak and the (311) austenite (γ) peaks are presented across all treatments for conditions F and D. The selection of these specific peaks is deliberate since the (311)γ response to stress and strain closely reflects the bulk behavior of austenite [33,34]; and the (211)α' peak presents lower elastic anisotropy factor in comparison to the (200)α' reflection [33]. Therefore, the intensity of the (211)α' peak will be less susceptible to the influence of crystallographic texture, which is an important aspect of the D condition. Figure 2a, c, e, and g show in situ results

throughout the entire heating and isothermal stages, while Figure 2b, d, f, and h focus on the first 60 s of heat treatment.

The comparative analysis of austenite quantification results (Figure 1) and martensite FWHM values (Figure 2a and b) reveals a notable correlation, suggesting that the austenite formation and growth result in a reduction in FWHMα' values. Wider diffraction peaks, i.e., larger FWHM values, have been related to increased density of crystalline defects, predominantly dislocations [35,36].

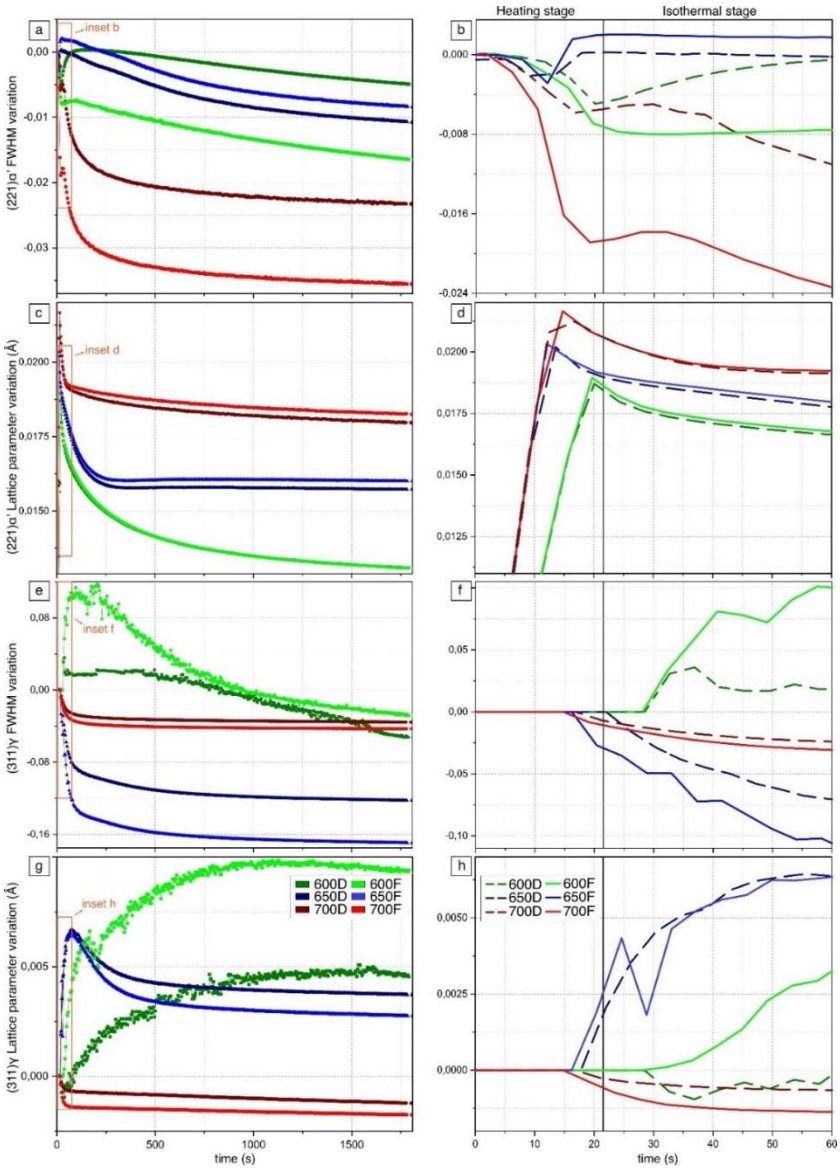

Figure 2 - Variation of FWHM based on (211)α' (a and b) and (311)γ (e and f) for the heating stage and isothermal step. And lattice parameter variation based on (211)α' (c and d) and (311)γ (g and h) also for

the heating stage and isothermal step. The three isothermal temperatures are plotted on the graphs for the F and D conditions: 600 °C (green), 650 °C (blue), and 700 °C (red).

The reduction in FWHMα' values at the onset of the thermal treatments during the heating stage can be attributed to the temperature rise, which will trigger the matrix's recovery through dislocation recombination. However, the fast heating rate of 50 °C.s^{-1} restricts the available time for recovery before phase transformations take place. In this manner, local strain fields in the martensitic matrix due to defects and/or precipitation, in the case of this study, can be an additional driving force for reverted austenite formation [18].

The variation of FWHMα' values, during the extended isothermal stage, follows a behavior remarkably similar to the inverse austenite reversion kinetics at each overaging temperature. In Figure 2c and d, the lattice parameter variation for the (211)α' peak is illustrated. Initially, the martensite lattice parameter increases due to thermal dilation upon heating. Then, a reduction in the lattice parameter values becomes evident just before the onset of the isothermal stage. Notably, at higher treatment temperatures, less decrease in the values and stabilization occur along the isothermal stage. These correlations are also associated with the diffusion of substitutional elements, such as Ni, Ti, and Mo, from the matrix toward austenite and precipitates, inducing martensite desaturation. The diffusion of those elements toward reverted austenite has been shown by Dmitrieva et. al. in a maraging-TRIP steel [37].

The austenite FWHM variation is depicted in Figure 2e and f. During overaging at 600 °C (F and D conditions), an initial increase followed by a progressive decrease occurs, which can indicate a very fine initial formation of austenite. This assumption is grounded in the fact that a small volume fraction and a fine phase size will manifest at the XRD pattern as short and thick peaks, resulting in higher FWHM values [36].

Consequently, higher volumes of austenite with fewer defects will present more intense and thinner peaks, i.e., lower FWHM values. This behavior is notable at higher temperatures, 650 and 700 °C, where the FWHMγ values decrease with austenite growth. A reduction in defect density with austenite reversion, as shown along the isothermal stage (Figure 2e), also indicates that austenite forms via diffusional transformation, since otherwise adiffusional austenite reversion should present high level of dislocation density, as shown by Tomimura et. al. [13].

The behavior of austenite lattice parameter variation (Figure 2g and h) could be related to compositional variations over time. Given that CALPHAD simulations indicate austenite forms with a high concentration of alloying, which tends to homogenize over time [18,37,38]. Therefore, an initial large lattice parameter followed by subsequent reduction over time can be expected during overaging, especially under slow reversion kinetics at 600 °C.

Figure 3 shows the dilation behavior during the heating stage for the F (Figure 3a) and D conditions (Figure 3c). Figure 3b presents the isothermal stage for all conditions, while Figure 3d focuses on the initial 180 s of the isothermal stage. In general, a noticeable contraction is evident across all heat-treating temperatures, with a more pronounced effect at the onset of the isothermal step. However, for both conditions treated at 650 ºC, there is a region (25 - 500 s) where the contraction rate changes, resulting in a distinct curve format. Another different behavior pertains to the 700D condition, which depicts an expansion stage right after 30 s of isothermal overaging.

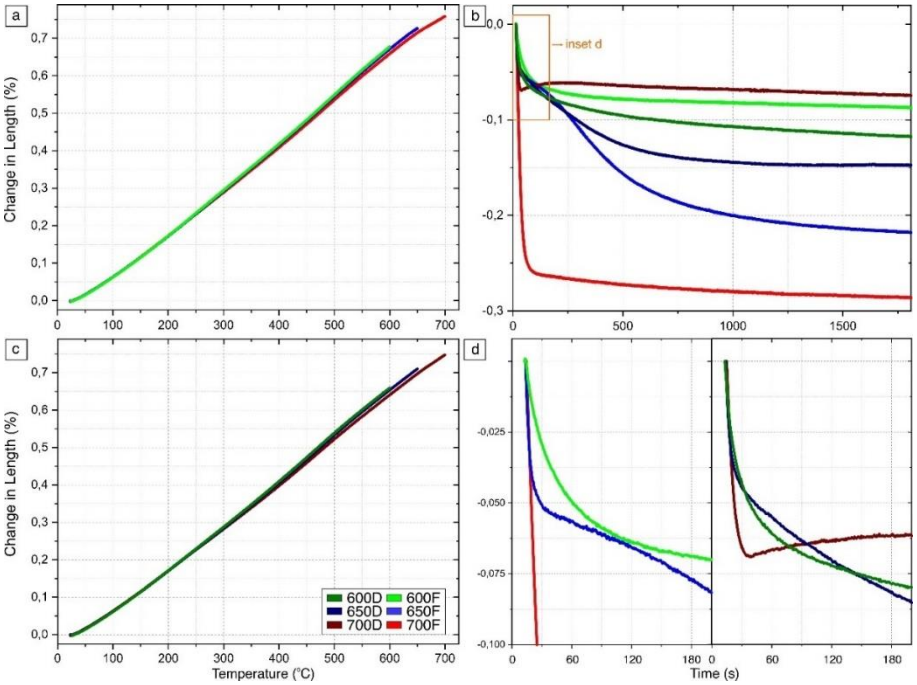

Figure 3 – Evolution of dilation during the heating stage (a and c) and the isothermal stage (b and d) for the three treatment temperatures, showing the undeformed (F) conditions and the cold rolled (D) conditions.

Similar to the SXRD results for the martensite matrix, the inverse relationship was observed between austenite formation (Figure 1) and volumetric dilation behavior (Figure 3b), due to austenite reversion, as the FCC structure is inherently more compact and denser than BCC martensite. Thus, the formation of reverted austenite induces contraction in the samples. Higher heat-treating temperatures lead to higher amounts of reverted austenite and, subsequently, a more pronounced volumetric contraction. However, even with the highest amount of austenite the 700D condition did not present the greatest contraction, which does not relate to any obvious explanation and requires further investigations.

Microstructural characterization via TEM and EBSD for the 600F condition is presented in Figure 4. In the bright field (BF) image (Figure 4a), the contrast between the matrix and the austenite is delineated by the dashed yellow lines. The dark field (DF) image (Figure 4b) evidences the precipitates in the martensitic matrix, primarily

appearing in rod and circular shapes. Selected Area Diffraction Pattern (SADP) results in Figure 4 (subsets $_{1, 2, 3}$ and $_{4}$) depict two types of secondary precipitates: rod-shaped $Ni_3(Ti, Mo)$ and circular Fe_2Mo. Similar precipitate morphologies and structures have been reported elsewhere [22,23,39]. The yellow circles in the first SADP of Figure 4($_1$) indicate austenite reflections, while the blue ones correspond to martensite. The crystallographic relationship between austenite and martensite was identified as Kurdjumov-Sachs, as reported by Viswanathan et. al. [23].

Figure 4($_3$ and $_4$) present, respectively, the SAD patterns of the martensitic matrix in two different zone axes, [001]α' and [011]α'. From these patterns, specific reflections were selected and the respective DF images in Figure 4c and e evidence the presence of secondary phases in the matrix. Both images show a morphology that matches the Ni_3Ti phase. The EBSD map in Figure 4f depicts austenite in green growing in between contours in agreement with the BF observations in Figure 4a.

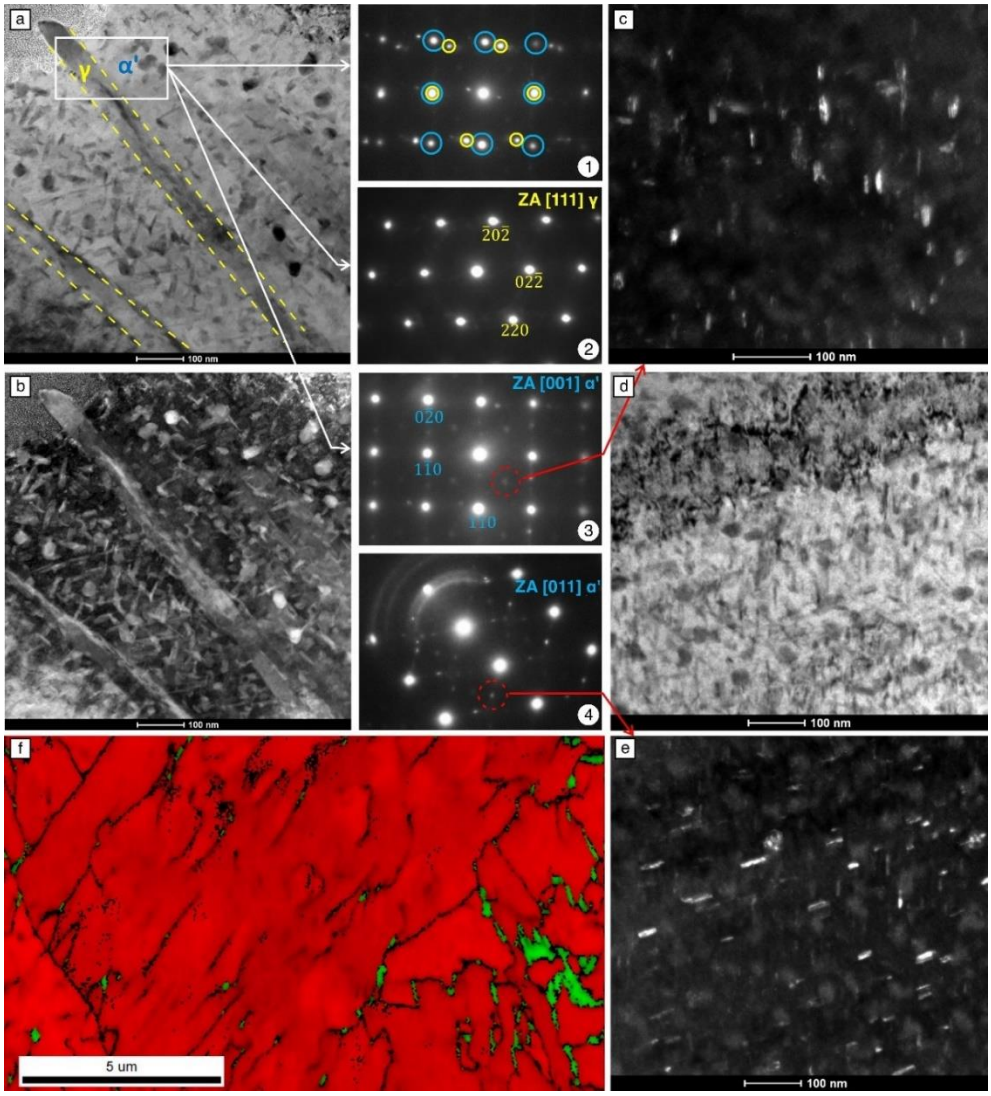

Figure 4 - TEM images of non-deformed condition treated at 600 °C (600F) showing: (a) BF with austenite highlighted with yellow lines and (b) DF image; (1, 2, 3 and 4) SADP taken at regions in the white rectangle in (a); (c) DF of the selected reflection in red of the diffraction pattern 3; (d) BF of the image (e); (e) DF of the selected reflection in red of the diffraction pattern 4. (f) EBSD of the 600F condition with phase contrast where γ is green and α' is red. The step size used was 50 nm.

The Energy Dispersive X-ray Spectroscopy (EDS) and APT results for the condition 600F are illustrated in Figure 5. In Figure 5a, EDS maps for Co, Fe, Mo, Ni and Ti are displayed for the region highlighted in the yellow square of the first image. The elongated phase in the upper right corner, highlighted with dashed yellow lines, exhibits lower concentrations of Co and Fe and higher concentrations of Mo and Ni. This phase is identified as interlath reverted austenite. The Fe map reveals the presence of fine precipitation zones depleted in this element, but rich in Ni and Ti (some

examples are highlighted with red arrows). These small rod-shaped phases are homogeneously distributed and were identified as Ni_3Ti. Also, the Mo map shows coarser and circular Mo-rich precipitates identified as Fe_2Mo. Additionally, some regions in austenite exhibit higher Mo concentrations, indicating that the austenite formation can occur in the vicinity of Fe_2Mo. There is no clear evidence of secondary precipitates inside the austenite laths via TEM-EDS.

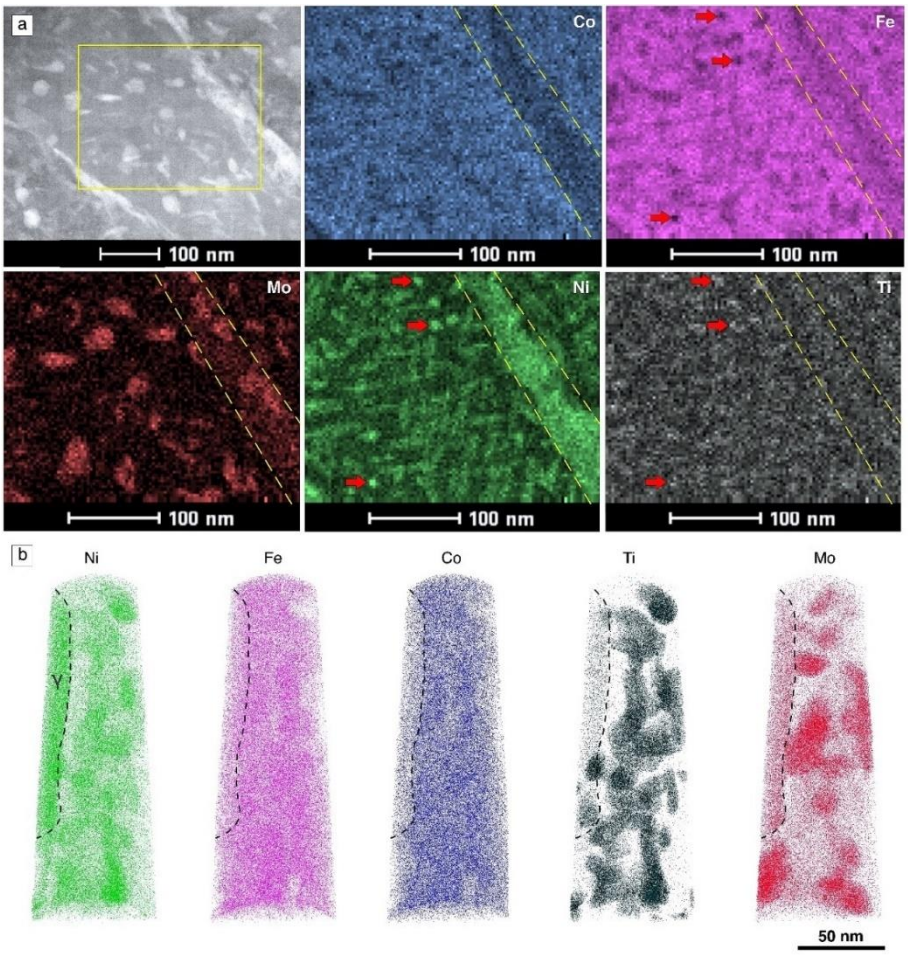

Figure 5 - EDS maps of elements from the selected area shown in (a) for the condition 600F. The elements are indicated at the upper part of the maps. Lighter regions mean a higher concentration of the displayed element. (b) APT reconstruction of each element for condition 600F.

In Figure 5b, APT tip reconstruction of the 600F condition is presented. The region on the left part of the tip, highlighted by a dashed black line, is enriched in Ni, Ti, and Mo, while slightly depleted in Fe and Co. This region has a local composition of 54.5Fe-23.4Ni-8.7Co-0.7Ti-2.9Mo (at.%), which is consistent with the composition of

austenite, as calculated by the CALPHAD method [19]. Also, outside austenite, Ti- and Mo-rich regions were identified as Ni_3Ti and Fe_2Mo, respectively.

The 3D reconstructions of the APT needle and proxigrams for the 600F sample is shown in Figure 6. The Ni ion distribution and iso-surfaces of 30 at.% Ni are in green in Figure 6a, evidencing the Ni_3Ti precipitates. A grey particle, indicated by the black box, was arbitrarily selected for analysis by constructing the proxigram on the right. This diagram delineates the variation in element concentration outside and inside the selected particle. The vertical black line positioned at zero indicates the iso-surface interface. Negative values along the horizontal axis denote the region external to the particle, while positive values represent the internal region of the particle in the direction toward its core. Following the computation of the average element concentrations within the particle, its composition was determined to be 56.6Ni-16.2Ti-1.5Mo-4.4Fe-4.1Co (at.%), approximately corresponding to the stoichiometry of Ni_3(Ti, Mo) with some substitution of Ni for Fe and Co.

A similar analysis considering Mo ions and iso-surfaces of 10 at. % of Mo is presented in Figure 6b, depicted in red. A highlighted grey particle was used to construct the proxigram. The average element concentration inside this particle was determined to be 37.4Fe-29.0Mo-3.9Ni-5.2Co-0.5Ti (at. %), indicative of an approximate stoichiometry of Fe_2Mo with some substitution of Fe for Ni and Co. An analogous analysis was done for 600D condition, presenting similar results, which can be found in Figure S2 in the Supplementary material. The compositions of Ni- and Mo-rich particles analyzed in the 600D condition were 54.6Ni-16.1Ti-3.9Mo-5.6Fe-6.1Co (at. %) and 31.6Fe-23.6Mo-5.9Ni-4.8Co-0.3Ti (at. %), respectively.

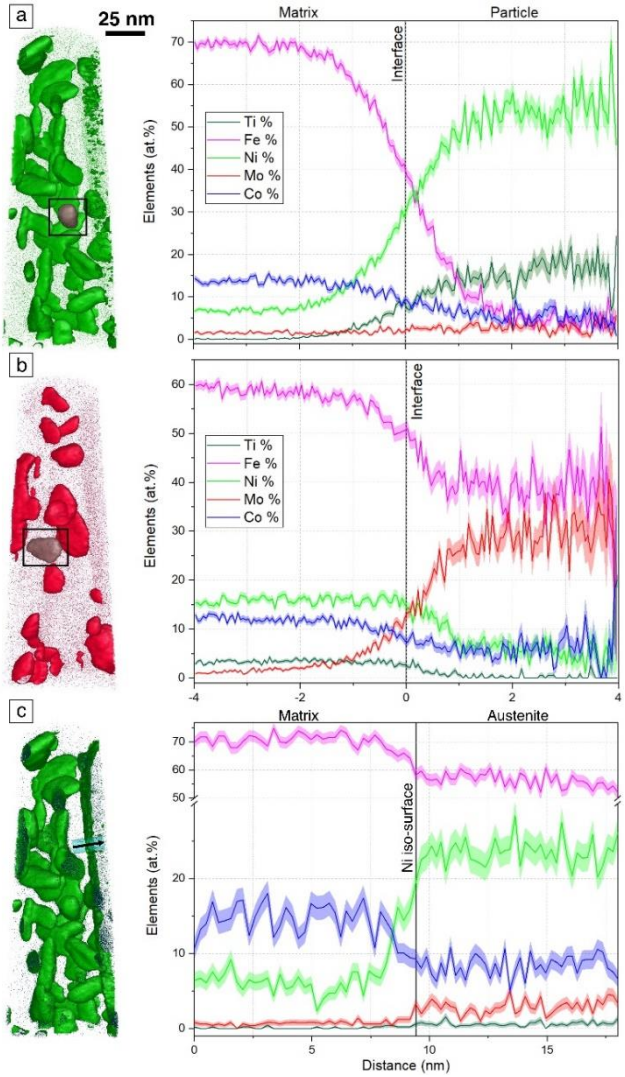

Figure 6 - APT reconstruction of sample 600F for (a) Ni ions depicting 30 at. % Ni and (b) Mo ions and 10 at. % Mo iso-surfaces, both with their respective proxigrams from the selected particle indicated by the black square; (c) Ti ions with 20 at. % Ni iso-surface with a ROI in blue showing the distribution of the elements in the graph at right.

Finally, Figure 6c presents the analysis with Ti ions in dark green and 20 at. % Ni iso-surface in green. A region of interest (ROI) delineated in blue was positioned at the interface between the matrix and the austenite. The elements distribution along the ROI is presented on the graphic at right. Notably, the austenite phase is enriched in Ni, Mo, and Ti, while depleted in Fe and Co. The Ni distribution between the matrix and austenite aligns with the simulated distribution shown by Santos et. al. [18].

Upon comparing the matrix composition across the three presented proxigrams, this phase is depleted in Fe around Mo-rich particles and depleted in Ni around Ni-rich

particles and γ. Overall, the matrix is depleted in Mo, with this element migrating to Mo-rich precipitates and austenite.

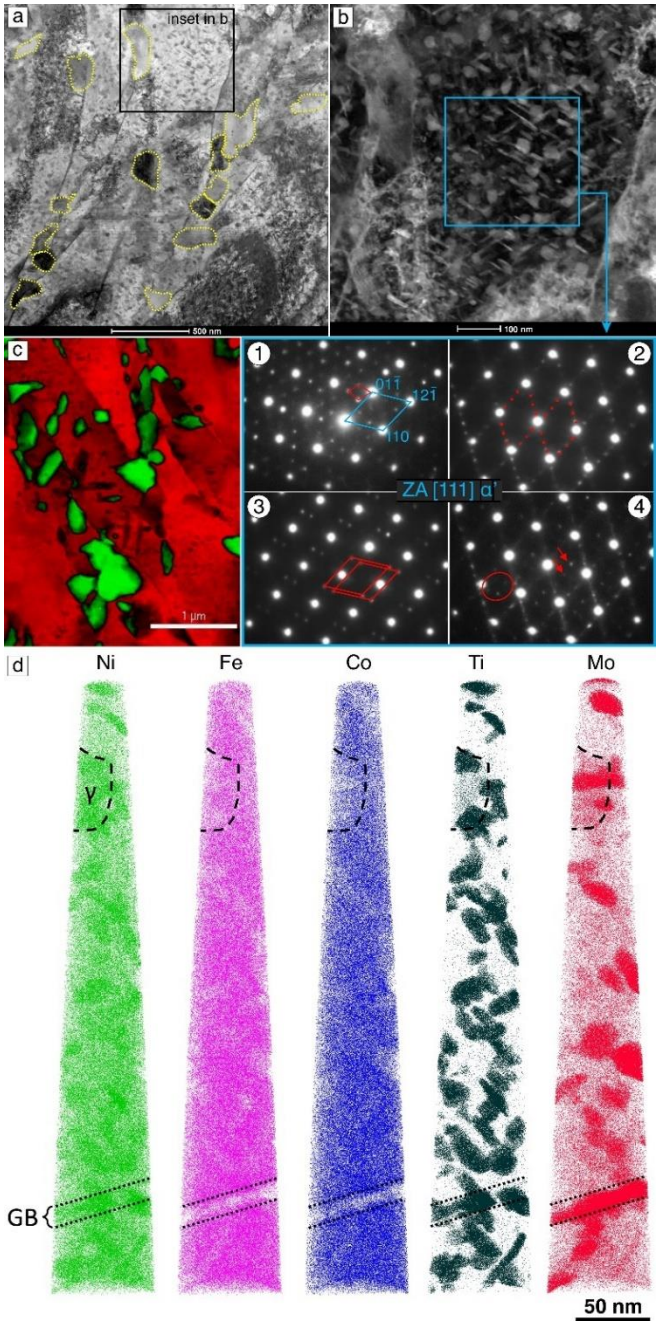

Figure 7 – TEM images from the same condition, showing the BF mode (a) and DF mode from a selected area (b). Nanobeam diffraction patterns (1, 2, 3 and 4) at the ZA[111]α' from the region highlighted in blue on (b). ASTAR crystallographic analysis from condition 600D with the phase map (c), showing austenite in green and matrix in red. (d) APT reconstruction showing the distribution of the elements with γ and a grain boundary (GB) delineated by dashed lines.

Figure 7 presents TEM and diffraction orientation mapping (ASTAR) results for the 600D condition. From the BF and DF images (Figure 7a and b), multiple

precipitates within the martensite laths with elongated or round shapes can be seen. Similar to the 600F sample, the elongated precipitates were identified as Ni_3Ti, while the coarser and rounder ones were identified as Fe_2Mo. The BF image further displays austenite indicated by yellow contours, exhibiting a distinct recrystallized and rounder morphology relative to that observed in the 600F case. This morphology of γ has already been described and classified in maraging 350 steel by Viswanathan et al. [23] after long overaging treatments, such as 640 °C for 8 hours.

The SADP ($_{1, 2, 3,}$ and $_4$ in Figure 7) show the martensitic matrix reflections at the ZA[111], along with weaker reflections related to multiple precipitates. In some SADP, such as the one numbered 4, the precipitate-matrix crystallographic relationship is not as clear. This lack of clarity can be attributed to overaging, during which the precipitates coalesce and lose coherence with the matrix, as noted by Mahadevan et. al. [35]. In the ASTAR phase map (Figure 7c), austenite is represented in green and the matrix in red, evidencing recrystallized austenite morphologies in between martensite laths.

The APT reconstruction is depicted in Figure 7d. Fe and Co appear homogeneously distributed and evident localized higher concentrations of Ni, Ti, and Mo are visible. A delimited region near the apex (delineated by a black dashed line) showed a local composition of 57.6Fe-28.9Ni-7.3Co-0.7Ti-2.6Mo (at. %), which is related to reverted austenite. Additional APT measurement from this condition with a higher volume fraction of austenite can be found in Figure S3 in the Supplementary Material. The reverted austenite block in the 600D condition is richer in Ni (28.9 at. %) than 600F condition (23.4 at. %). Plastic deformation increases the dislocation density, and therefore, pipe diffusion of gamma-stabilizer elements is assisted [32]. The bottom

part of the tip presents a grain boundary region enriched in Mo, consistent with the observations from Niu et al. [40].

A comparative summary of APT reconstructions from the three temperatures of treatment for F and D conditions is illustrated in Figure 8, showing Ti ions and iso-surfaces of 23 at. % Ni (green) and 10 at. % Mo (red) to highlight the distribution and morphology of Ni_3Ti and Fe_2Mo particles, respectively.

The effect of cold rolling can be more clearly seen when comparing overaging conditions at 600 °C. Both Ni_3Ti and Fe_2Mo particles present in the 600D condition are smaller, while a higher density of precipitation is also evident when compared to 600F. This is due to more nucleation sites being available in the deformed condition. In the 650 °C samples, the Ni_3Ti precipitates exhibit larger dimensions, while at 700 °C dissolution is taking place, evidenced by reduced particle size and number. Furthermore, the proximity of Ni_3Ti and Fe_2Mo particles, bellow 650 °C, suggests potential cooperation during nucleation and growth, facilitating Fe_2Mo formation, in line with suggestions by other authors [1,41]. At higher temperatures, the dissolution of those precipitates is favored along the isothermal stage, supporting the austenite growth by diffusion of the elements released from the precipitates' dissolution, a phenomenon corroborated by thermodynamic analysis in previous work [19].

The presence of intermetallic precipitates inside austenite after overaging at 700 °C (F and D cases) indicates the rapid advance of the austenite interface, enveloping intermetallic precipitates previously nucleated within martensite. Only approximately 0.1 volume fraction of martensite is left untransformed after 1800 s of overaging. According to Schnitzer et al. [12] dissolution of Ni-Al precipitates in PH

maraging steel can occur around the austenite areas, with Ni diffusing into austenite after precipitate dissolution, promoting growth.

The homogeneous distribution of Ti along the tip intensifies with the rise in treatment temperature, as indicated by the Ti ions (dark-green points). Austenite was detected in all samples and is denoted by the γ symbol in the 600 and 650 °C measurements. In 700F, the martensite (α') region is highlighted (Figure 8a), as the remainder of the tip is austenite and precipitates. The austenite composition for all conditions is summarized in Table 2. The austenite observed is rich in Ti ions, yet some small Ni-Ti-rich precipitates persist.

At 650F, the size of Mo-rich precipitates near the austenite is smaller than those farther away from this phase. This observation suggests that element dissolution occurs toward the austenite, or alternatively, the austenite grows towards regions where dissolution occurs fast. Given that faster dissolution can occur in areas with higher dislocation density, defects, boundaries, and contours, and considering the preference for austenite growth in such defect-rich regions, a faster dissolution near the austenite is plausible.

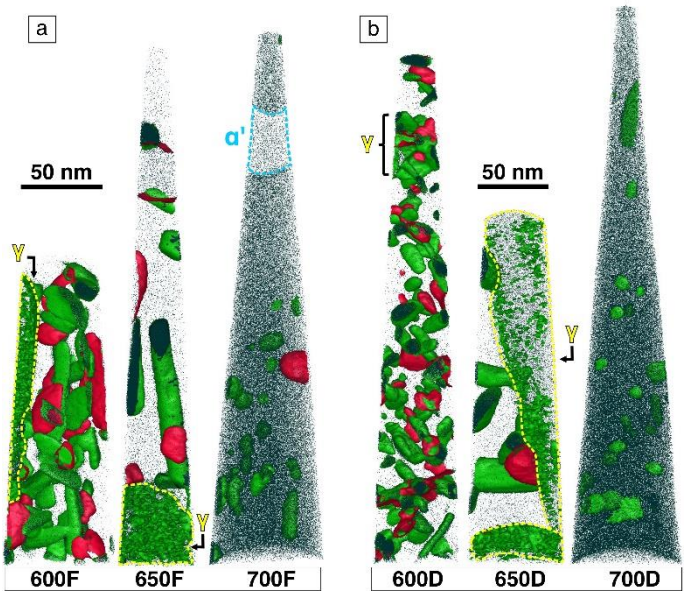

Figure 8 - APT reconstruction for all conditions showing iso-surfaces of 23 at. % Ni (green) and 10 at. % Mo (red), also Ti atoms are shown in dark green.

Although Ni_3Ti and Fe_2Mo precipitates were identified, it should be noted that their stoichiometries were identified as $(Ni,Fe,Co)_{3.7}(Ti,Mo)$ and $(Fe,Ni,Co)_{1.6}(Mo,Ti)$, respectively. Such stoichiometric deviations have already been discussed in a detailed study of a maraging 250 steel conducted by Vasudevan et al. [42], where the intermetallic precipitates were characterized crystallographically and compositionally, and the reported average stoichiometry for Ni_3Ti was $(Ni,Fe)_{3.6}(Ti,Mo)$, and for Fe_2Mo was $(Fe,Ni,Co)_2(Mo,Ti)$.

The shape factors of the Ni-rich precipitates were computed based on the results presented in Figure 8 and were determined to be 4.37, 7.14, and 1.13 for the 600F, 650F, and 700F conditions, respectively. Comparatively, for the 600D and 700D conditions, the shape factors were 2.03 and 1.03, respectively. Notice that it was not feasible to calculate the shape factor for the 650D condition, as no precipitate was found entirely within the analyzed needle. Concerning the Mo-rich precipitates, the shape factors were 1.47 (600F) and 1.06 (600D), while it was not possible to calculate these values for the remaining conditions.

Table 2 – Austenite composition for all treatment conditions in at. %, measured from APT results.

	Fe	**Ni**	**Co**	**Ti**	**Mo**
600F	54.5	23.4	8.7	0.7	2.9
600D	64.2	24.9	6.3	0.4	3.1
650F	59.0	22.4	9.6	0.8	2.4
650D	63.7	19.1	9.7	0.7	2.6
700F	67.0	13.0	9.5	1.1	2.8
700D	60.9	14.5	9.7	1.4	2.3

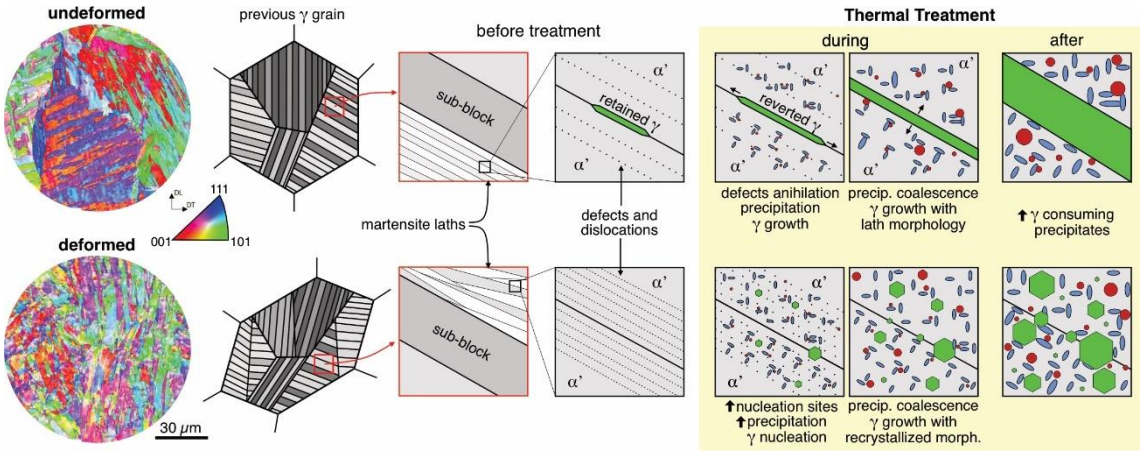

Figure 9 – Illustrated scheme of the proposed sequence of phase transformations on maraging 350 steel.

A proposed schematic representation of the evolution of phase transformations during the overaging of the material is illustrated in Figure 9. Finer intermetallic particles with a higher precipitation density, as well as more equiaxed reverted austenite will form during overaging in a plastically deformed matrix. We suggest that austenite grows around the precipitates surrounding them and then continues to grow towards the martensite regions. In contrast, the dissolution of elements from the precipitates occurs concurrently. Hence, we propose that the precipitates cooperate with the austenite nucleation. Nevertheless, reverted austenite growth occurs to the detriment of precipitates, with the final dissolution stage of intermetallics happening inside the austenite. In this context, could we still call this “cooperation”? To elucidate this mechanism, further investigation with Small-Angle X-Ray Scattering (SAXS) is recommended to analyze the first stage of reverted austenite nucleation.

4. Conclusions

The sequences of austenite reversion and secondary precipitation in a maraging 350 steel were studied via synchrotron X-ray diffraction and dilatometry for different conditions (undeformed and cold rolled 50 % in width) during in situ overaging treatments (600 – 700 °C for 1800 s). The material microstructure after the heat

treatments was analyzed through advanced microstructural characterization using TEM and APT.

The precipitates identified by TEM and APT were Fe_2Mo, characterized by a typical rounded morphology, and Ni_3Ti, displaying a rodded/elongated shape. These precipitates exhibited a certain degree of atom substitution, with stoichiometries determined as $(Fe, Ni, Co)_{1.6}(Mo, Ti)$ and $(Ni, Fe, Co)_{3.7}(Ti, Mo)$, respectively.

In situ synchrotron X-ray diffraction data showed that the reverted austenite nucleation/formation induces microstrain in the martensitic matrix, but its further growth induced overall relaxation of the martensitic matrix due to recovery. This technique also clarified that, controversially, the presence of cold rolling deformation did not significantly alter the kinetics of austenite reversion nor the volume fraction of reverted austenite after the isothermal heat treatments. However, the austenite kinetics was helped by the retained austenite present in the undeformed condition, which was not present in the deformed condition. Additionally, the morphology of the reverted austenite is very different for each condition, as revealed by TEM. It is aligned with the interlath boundary for the undeformed condition, while obtaining an equiaxed and recrystallized morphology in the deformed condition, although the total volume is not different.

The cold rolling condition did enhance phase transformation in maraging 350 steel, although it was not the reverted austenite transformation, at least not directly. The SXRD and APT results independently showed that the presence of deformation favored precipitation, since Ni_3Ti and Fe_2Mo exhibited finer sizes and a higher precipitation density after plastic deformation. The precipitates subsequently coalesced and partially dissolved at elevated temperatures (650 and 700 °C, respectively), thereby supporting

austenite growth through the diffusion of elements liberated during the dissolution process. By this, it is suggested that the austenite nucleation occurred with the cooperation of the precipitates, while further austenite growth occurred in the depletion of the precipitates.

Our findings are useful for the future design of more efficient overaging heat treatments aiming secondary particle size control via thermo-mechanical processing. Cold rolling offers the possibility to maintain smaller precipitate sizes and large precipitation densities while having a limited effect on the kinetics of austenite reversion.

Acknowledgments

We acknowledge DESY (Hamburg, Germany), a member of the Helmholtz Association HGF, for providing the experimental facilities. Parts of this research were carried out at PETRA III, and we would like to thank Emad Maawad and Norbert Schell for their assistance in using the P07 beamline. Beamtime was allocated for proposal I-20191506. The authors thank the Laboratory of Structural Characterization (LCE/DEMa/UFSCar) for the general facilities. This research used facilities of the Brazilian Nanotechnology National Laboratory (LNNano), part of the Brazilian Centre for Research in Energy and Materials (CNPEM), a private non-profit organization under the supervision of the Brazilian Ministry for Science, Technology, and Innovations (MCTI). The Microscopia eletrônica staff is acknowledged for the assistance during the experiments (proposal # TEM-C1 - 27214). The authors thank the Karlsruhe Nano and Micro Facility (KNMFi), a Helmholtz Research Infrastructure at Karlsruhe Institute of Technology (KIT) for the usage of Atom Probe Tomograph (APT) equipment and the assistance of Marina Weinhard and Delphine Chassaing in producing the samples for APT. Authors from the USP Polytechnic School would like to thank the Coordenação de Aperfeiçoamento de Pessoal de Nível Superior (CAPES) - Programa de Excelência Acadêmica (PROEX) - Brasil for Financial Support. We especially acknowledge Felipe Moreno Siqueira Borges de Carvalho for conducting the cold rolling process at the IPT – USP. J. Avila is a Serra Hunter fellow and a CNPq fellow. JPO acknowledges funding by national funds

from FCT - Fundação para a Ciência e a Tecnologia, I.P., in the scope of the projects LA/P/0037/2020, UIDP/50025/2020 and UIDB/50025/2020 of the Associate Laboratory Institute of Nanostructures, Nanomodelling and Nanofabrication – i3N.

References

[1] K. Rohrbach, M. Schmidt, C.T. Corporation, Maraging Steels, in: Prop. Sel. Irons, Steels, High-Performance Alloy., ASM International, 1990: pp. 793–800. https://doi.org/10.31399/asm.hb.v01.a0001043.

[2] S. Loewy, B. Rheingans, S.R. Meka, E.J. Mittemeijer, Unusual martensite-formation kinetics in steels: Observation of discontinuous transformation rates, Acta Mater. 64 (2014) 93–99. https://doi.org/10.1016/j.actamat.2013.11.052.

[3] H. Shirazi, G. Miyamoto, S. Hossein Nedjad, T. Chiba, M. Nili Ahmadabadi, T. Furuhara, Microstructure evolution during austenite reversion in Fe-Ni martensitic alloys, Acta Mater. 144 (2018) 269–280. https://doi.org/10.1016/j.actamat.2017.10.068.

[4] M. Schmidt, K. Rohrbach, C. Carson, Heat Treating of Maraging Steels, in: Heat Treat. Irons Steels, ASM International, 2014: pp. 468–480. https://doi.org/10.31399/asm.hb.v04d.a0005948.

[5] D.P.M. da Fonseca, A.L.M. Feitosa, L.G. de Carvalho, R.L. Plaut, A.F. Padilha, A Short Review on Ultra-High-Strength Maraging Steels and Future Perspectives, Mater. Res. 24 (2021) 1–11. https://doi.org/10.1590/1980-5373-mr-2020-0470.

[6] W. Sha, Z. Guo, Maraging steels: Modelling of microstructure, properties and applications, Woodhead Publishing, Nova York, 2009. https://doi.org/10.1533/9781845696931.

[7] B. Rohit, N.R. Muktinutalapati, Austenite reversion in 18% Ni maraging steel and its weldments, Mater. Sci. Technol. 34 (2018) 253–260. https://doi.org/10.1080/02670836.2017.1407544.

[8] S. Floreen, The physical metallurgy of maraging steels, Metall. Rev. 13 (1968) 115–128. https://doi.org/10.1179/mtlr.1968.13.1.115.

[9] A. Markfeld, A. Rosen, Effect of Reverted Austenite on the Plastic Deformation of Maraging Steel., Mater. Sci. Eng. 46 (1980) 151–157. https://doi.org/10.1016/0025-5416(80)90171-8.

[10] F. Tariq, R.A. Baloch, B. Ahmed, N. Naz, Investigation into Microstructures of Maraging Steel 250 Weldments and Effect of Post-Weld Heat Treatments, J. Mater. Eng. Perform. 19 (2010) 264–273. https://doi.org/10.1007/s11665-009-9455-1.

[11] U.K. Viswanathan, G.K. Dey, V. Sethumadhavan, Effects of austenite reversion during overageing on the mechanical properties of 18 Ni (350) maraging steel, Mater. Sci. Eng. A. 398 (2005) 367–372. https://doi.org/10.1016/j.msea.2005.03.074.

[12] R. Schnitzer, R. Radis, M. Nöhrer, M. Schober, R. Hochfellner, S. Zinner, E. Povoden-Karadeniz, E. Kozeschnik, H. Leitner, Reverted austenite in PH 13-8 Mo maraging steels, Mater. Chem. Phys. 122 (2010) 138–145. https://doi.org/10.1016/j.matchemphys.2010.02.058.

[13] K. Tomimura, S. Takaki, Y. Tokunaga, Reversion Mechanism from Deformation

Induced Martensite to Austenite in Metastable Austenitic Stainless Steels., ISIJ Int. 31 (1991) 1431–1437. https://doi.org/10.2355/isijinternational.31.1431.
[14] M.C. Somani, P. Juntunen, L.P. Karjalainen, R.D.K. Misra, A. Kyröläinen, Enhanced Mechanical Properties through Reversion in Metastable Austenitic Stainless Steels, Metall. Mater. Trans. A. 40 (2009) 729–744. https://doi.org/10.1007/s11661-008-9723-y.
[15] J.D. Escobar, G.A. Faria, L. Wu, J.P. Oliveira, P.R. Mei, A.J. Ramirez, Austenite reversion kinetics and stability during tempering of a Ti-stabilized supermartensitic stainless steel: Correlative in situ synchrotron x-ray diffraction and dilatometry, Acta Mater. 138 (2017) 92–99. https://doi.org/10.1016/j.actamat.2017.07.036.
[16] A. Ali, M. Ahmed, F.H. Hashmi, A.Q. Khan, Austenite reversion in cold formed 18 wt-%Ni 350 grade maraging steel, Mater. Sci. Technol. 10 (1994) 97–101. https://doi.org/10.1179/mst.1994.10.2.97.
[17] L.G. de Carvalho, M.S. Andrade, R.L. Plaut, F.M. Souza, A.F. Padilha, A dilatometric study of the phase transformations in 300 and 350 maraging steels during continuous heating rates, Mater. Res. 16 (2013) 740–744. https://doi.org/10.1590/S1516-14392013005000069.
[18] L.P.M. dos Santos, M. Béreš, M.O. de Castro, P.W.C. Sarvezuk, L. Wu, L.F.G. Herculano, A. Paesano, C.C. Silva, M. Masoumi, H.F.G. de Abreu, Kinetics of Reverted Austenite in 18 wt.% Ni Grade 300 Maraging Steel: An In-Situ Synchrotron X-Ray Diffraction and Texture Study, Jom. 72 (2020) 3502–3512. https://doi.org/10.1007/s11837-020-04254-w.
[19] A.L.M. Feitosa, J. Escobar, G.G. Ribamar, J.A. Avila, A.F. Padilha, Direct Observation of Austenite Reversion During Aging of 18Ni (350 Grade) Maraging Steel Through In-Situ Synchrotron X-Ray Diffraction, Metall. Mater. Trans. A. 53 (2022) 420–431. https://doi.org/10.1007/s11661-021-06496-y.
[20] J.M. Pardal, S.S.M. Tavares, V.F. Terra, M.R. Da Silva, D.R. Dos Santos, Modeling of precipitation hardening during the aging and overaging of 18Ni-Co-Mo-Ti maraging 300 steel, J. Alloys Compd. 393 (2005) 109–113. https://doi.org/10.1016/j.jallcom.2004.09.049.
[21] F.F. Conde, J.A. Avila, J.P. Oliveira, N. Schell, M.F. Oliveira, J.D. Escobar, Effect of the as-built microstructure on the martensite to austenite transformation in a 18Ni maraging steel after laser-based powder bed fusion, Addit. Manuf. 46 (2021) 102122. https://doi.org/10.1016/j.addma.2021.102122.
[22] O. Moshka, M. Pinkas, E. Brosh, V. Ezersky, L. Meshi, Addressing the issue of precipitates in maraging steels – Unambiguous answer, Mater. Sci. Eng. A. 638 (2015) 232–239. https://doi.org/10.1016/j.msea.2015.04.067.
[23] U.K. Viswanathan, G.K. Dey, M.K. Asundi, Precipitation hardening in 350 grade maraging steel, Metall. Trans. A. 24 (1993) 2429–2442. https://doi.org/10.1007/BF02646522.
[24] G.A. Faria, Exploring Metallic Materials Behavior Through In Situ Crystallographic Studies by Synchrotron Radiation, University of Campinas, 2014. http://repositorio.unicamp.br/jspui/handle/REPOSIP/265849.
[25] A. Bojack, L. Zhao, P.F. Morris, J. Sietsma, In-situ determination of austenite and martensite formation in 13Cr6Ni2Mo supermartensitic stainless steel, Mater. Charact. 71 (2012) 77–86. https://doi.org/10.1016/j.matchar.2012.06.004.
[26] M.K. Miller, Atom Probe Tomography and the Local Electrode Atom Probe,

2004. https://doi.org/10.1017/S1431927604881157.
[27] W. Lefebvre-Ulrikson, F. Vurpillot, X. Sauvage, Atom Probe Tomography: Put Theory into Practice, 2016. https://www.sciencedirect.com/book/9780128046470/atom-probe-tomography#book-description.
[28] L. Morsdorf, O. Jeannin, D. Barbier, M. Mitsuhara, D. Raabe, C.C. Tasan, Multiple mechanisms of lath martensite plasticity, Acta Mater. 121 (2016) 202–214. https://doi.org/10.1016/j.actamat.2016.09.006.
[29] F.F. Conde, J.D. Escobar, J.P. Oliveira, A.L. Jardini, W.W. Bose Filho, J.A. Avila, Austenite reversion kinetics and stability during tempering of an additively manufactured maraging 300 steel, Addit. Manuf. 29 (2019) 100804. https://doi.org/10.1016/j.addma.2019.100804.
[30] A. Behravan, A. Zarei-Hanzaki, S.M. Fatemi, H.F.G. De Abreu, M. Masoumi, The Effect of Aging Temperature on Microstructure and Tensile Properties of a Novel Designed Fe–12Mn–3Ni Maraging-TRIP Steel, Steel Res. Int. 90 (2019) 1800282. https://doi.org/10.1002/srin.201800282.
[31] M.-M. Wang, C.C. Tasan, D. Ponge, D. Raabe, Spectral TRIP enables ductile 1.1 GPa martensite, Acta Mater. 111 (2016) 262–272. https://doi.org/10.1016/j.actamat.2016.03.070.
[32] J. Tian, W. Wang, H. Li, M.B. Shahzad, Y. Shan, Z. Jiang, K. Yang, Effect of deformation on precipitation hardening behavior of a maraging steel in the aging process, Mater. Charact. 155 (2019) 109827. https://doi.org/10.1016/j.matchar.2019.109827.
[33] S. Ebner, R. Schnitzer, E. Maawad, C. Suppan, C. Hofer, Influence of partitioning parameters on the mechanical stability of austenite in a Q&P steel: A comparative in-situ study, Materialia. 15 (2021) 101033. https://doi.org/10.1016/j.mtla.2021.101033.
[34] B. Clausen, T. Lorentzen, T. Leffers, Self-consistent modelling of the plastic deformation of f.c.c. polycrystals and its implications for diffraction measurements of internal stresses, Acta Mater. 46 (1998) 3087–3098. https://doi.org/10.1016/S1359-6454(98)00014-7.
[35] S. Mahadevan, T. Jayakumar, B.P.C. Rao, A. Kumar, K. V. Rajkumar, B. Raj, X-ray diffraction profile analysis for characterizing isothermal aging behavior of M250 grade maraging steel, Metall. Mater. Trans. A Phys. Metall. Mater. Sci. 39 (2008) 1978–1984. https://doi.org/10.1007/s11661-008-9550-1.
[36] B.D. Cullity, Elements of X-ray Diffraction, 2nd ed., Addison-Wesley publishing company INC., Philippines, 1978.
[37] O. Dmitrieva, D. Ponge, G. Inden, J. Millán, P. Choi, J. Sietsma, D. Raabe, Chemical gradients across phase boundaries between martensite and austenite in steel studied by atom probe tomography and simulation, Acta Mater. 59 (2011) 364–374. https://doi.org/10.1016/j.actamat.2010.09.042.
[38] F. Niessen, M. Villa, J. Hald, M.A.J. Somers, Kinetics analysis of two-stage austenitization in supermartensitic stainless steel, Mater. Des. 116 (2017) 8–15. https://doi.org/10.1016/j.matdes.2016.11.076.
[39] R. Tewari, S. Mazumder, I.S. Batra, G.K. Dey, S. Banerjee, Precipitation in 18 wt% Ni maraging steel of grade 350, Acta Mater. 48 (2000) 1187–1200. https://doi.org/10.1016/S1359-6454(99)00370-5.
[40] M.C. Niu, C.J. Chen, W. Li, K. Yang, J.H. Luan, W. Wang, Z.B. Jiao, Atomic-

scale understanding of solute interaction effects on grain boundary segregation, precipitation, and fracture of ultrahigh-strength maraging steels, Acta Mater. 253 (2023) 118972. https://doi.org/10.1016/j.actamat.2023.118972.
[41] M. Niu, G. Zhou, W. Wang, M.B. Shahzad, Y. Shan, K. Yang, Precipitate evolution and strengthening behavior during aging process in a 2.5 GPa grade maraging steel, Acta Mater. 179 (2019) 296–307. https://doi.org/10.1016/j.actamat.2019.08.042.
[42] V.K. Vasudevan, S.J. Kim, C.M. Wayman, Precipitation reactions and strengthening behavior in 18 Wt Pct nickel maraging steels, Metall. Trans. A. 21 (1990) 2655–2668. https://doi.org/10.1007/BF02646061.